UNDER-RESOLUTION AND DIAGNOSTICS IN SPECTRAL SIMULATIONS OF COMPLEX-GEOMETRY FLOWS

Robert M. Kirby
Division of Applied Mathematics
Brown University
kirby@cfm.brown.edu

George Em Karniadakis
Division of Applied Mathematics
Brown University
gk@cfm.brown.edu

Abstract

Large-scale simulations are often under-resolved at some level, but they are still useful in extracting both qualitative and quantitative information about the flow. In order to use such results effectively we need to characterize the numerical uncertainty of under-resolved simulations. However, different numerical methods exhibit different behavior, and spectral-based methods in particular may over-predict fluctuations both in amplitude and frequency due to their very low artificial dissipation in contrast with finite differences. In this chapter, we provide insight into under-resolved spectral simulations and document several diagnostic signs of under-resolution for spectral/hp element methods. We first review the state-of-the art in direct numerical simulation and present a new class of spectral methods on unstructured grids for handling complex-geometry compressible and incompressible flows. We then focus on the effects of under-resolving the nonlinear contributions, and finally we present prototype cases for both transitional and turbulent flows.

Keywords: Spectral methods, complex-geometry, under-resolution, unstructured grids, turbulence

Report Documentation Page

Form Approved
OMB No. 0704-0188

1. REPORT DATE	2. REPORT TYPE	3. DATES COVERED
2001		**00-00-2001 to 00-00-2001**

4. TITLE AND SUBTITLE	5a. CONTRACT NUMBER
Under-Resolution and Diagnostics in Spectral Simulations of Complex-Geometry Flows	5b. GRANT NUMBER
	5c. PROGRAM ELEMENT NUMBER
6. AUTHOR(S)	5d. PROJECT NUMBER
	5e. TASK NUMBER
	5f. WORK UNIT NUMBER
7. PERFORMING ORGANIZATION NAME(S) AND ADDRESS(ES) **Brown University,Division of Applied Mathematics,182 George Street,Providence,RI,02912**	8. PERFORMING ORGANIZATION REPORT NUMBER
9. SPONSORING/MONITORING AGENCY NAME(S) AND ADDRESS(ES)	10. SPONSOR/MONITOR'S ACRONYM(S)
	11. SPONSOR/MONITOR'S REPORT NUMBER(S)

12. DISTRIBUTION/AVAILABILITY STATEMENT
Approved for public release; distribution unlimited

13. SUPPLEMENTARY NOTES
The original document contains color images.

14. ABSTRACT

15. SUBJECT TERMS

16. SECURITY CLASSIFICATION OF:			17. LIMITATION OF ABSTRACT	18. NUMBER OF PAGES	19a. NAME OF RESPONSIBLE PERSON
a. REPORT **unclassified**	b. ABSTRACT **unclassified**	c. THIS PAGE **unclassified**		**44**	

1. Introduction

Under-resolved simulations are perhaps the rule rather than the exception! This can be understood, as in practice users attempt high Reynolds number simulations in problems with new physics and thus unknown resolution requirements. Verification and validation of the solution is a very tedious process ([1]), and at present there are no established efficient methods to assess numerical accuracy. Also, for large-scale turbulence simulations, existing computational resources may often be inadequate for the attempted simulations, so additional error checking simulations would be prohibitively expensive.

However, an under-resolved simulation is not useless but, in fact, it can provide a lot of information if proper characterization is established combined with experience for the specific discretization used in such a simulation. One such example is a relatively early direct numerical simulation of turbulent channel flow by ([2]) which has remained largely unnoticed. In figure 1 we plot one of his results, i.e. the Reynolds stress distribution across the channel. It is in good agreement with high resolution DNS even for the lowest resolution employed in Zores's simulation, corresponding to four Fourier modes in the streamwise, 16 Chebyshev modes in the normal, and six Fourier modes in the spanwise direction. The Reynolds number based on the wall shear velocity is $R_* \approx 120$. In order to achieve smooth profiles a very long- time averaging was employed. Clearly, this is an example of an under-resolved simulation, which however sustains the turbulence fluctuations and leads to better than 10% accuracy in second-order statistics. In contrast, a low resolution simulation based on finite differences would typically converge to the laminar steady state solution.

For under-resolved simulations to be useful we need to characterize both numerical and physical uncertainty, creating appropriate composite error bars similar to experiments. This is a very difficult task, and work on uncertainty associated with the data, i.e. input, is still at an early stage. On the numerical side, there are still many classical issues which are unresolved today, e.g. skew-symmetry of advection operators in the discrete sense, time-integration algorithms with large time step, efficient treatment of geometric complexity, efficient adaptivity, etc.

There are two major challenges today in direct numerical simulations (DNS) of turbulence following the successes of the last two decades ([3]): The first is that the maximum Reynolds number possible in simulations is still much lower compared to turbulent flows of practical interest. For example, at present or in the near future, the maximum Re_λ (based on the Taylor micro-scale) for homogeneous turbulence that can be ac-

curately simulated is less than 500. However, in geophysical flows the typical Reynolds number Re_λ may be orders of magnitude higher. The second challenge we face is that complex-geometry flows are still largely untackled; geometries beyond the standard channel flow with flat walls have only recently been considered, and most of them involve at least one homogeneous direction.

A summary of the range of Reynolds number and geometries for which direct numerical simulations have been successfully completed is plotted in the sketch of figure 2. It shows that accurate direct numerical simulations of turbulence in simple-geometry domains can handle much higher Reynolds number flows than in complex-geometry domains. This, in essence, reflects the additional computational complexity associated with discretization of the Navier-Stokes equations in complex-geometry domains. Clearly, the Fourier discretization which is employed for all three directions in homogeneous turbulence cannot be used in inhomogeneous directions, where Chebyshev or Legendre spectral discretizations (or alternatively some high-order finite difference variant) are used. More specifically, on non-separable or multiply-connected domains (e.g. flow past a circular cylinder) these classical methods are also inappropriate, and thus new domain-decomposition based methods need to be used effectively.

As regards the type of discretization, it was evident even from the early attempts to perform DNS of turbulence in the seventies, that high-order discretization was not only computationally advantageous but

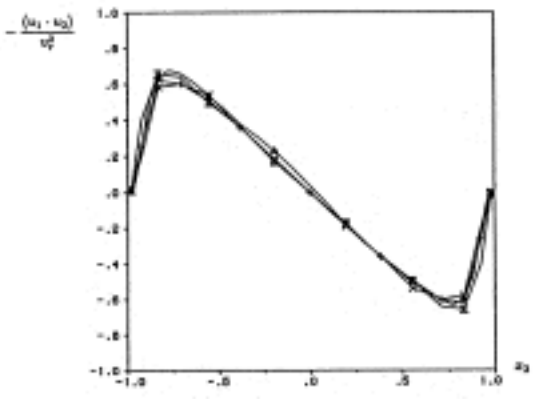

Figure 1. Reynolds stress distribution of a low-resolution simulation of a turbulent channel flow by ([2]). The different symbols correspond to different resolution in x (stream), y (normal) and z (span) as follows: $\triangle : 8\times32\times8$; $\bowtie$: $8\times16\times8$; $+ : 6\times16\times6$; $\times : 4\times16\times6$.

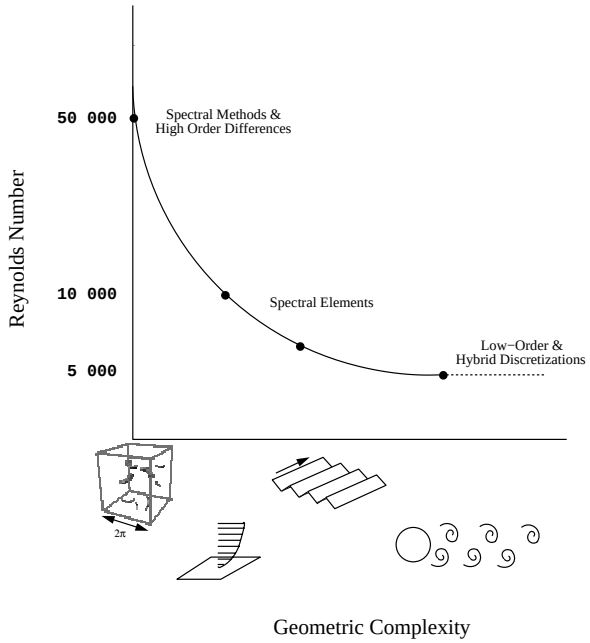

Figure 2. Conceptual overview of DNS of turbulent flows: Maximum Reynolds number versus geometric complexity.

also a necessity. Simulating turbulence requires long-time integration, however non-negligible dispersion errors associated with low-order discretization could eventually render the computational results erroneous. There is plenty of anecdotal evidence about such results from the early practitioners, and modern numerical analysis can rigorously document this as well. The importance of high-order discretization has also been recognized for large eddy simulations (LES) ([4]), as discretization errors seem to interact with the subgrid modeling errors in an adverse way.

As we go through the multi-Teraflop (and beyond) computing era and are capable of performing simulations of 1 billion points or more at reasonable turn-around time, high-order numerical methods will play a key role in simulating high Reynolds number and complex-geometry turbulence. They provide

- fast convergence,
- small diffusion and dispersion errors,
- easier implementation of the *inf-sup* condition for incompressible Navier-Stokes,

- better data volume-over-surface ratio for efficient parallel processing, and
- better input/output handling due to the smaller volume of data.

For many engineering applications where accuracy of the order of 10% is acceptable, quadratic convergence is usually sufficient for stationary problems. However, this is not true in time-dependent flow simulations where long-time integration is required. Also, in DNS a 10% inaccuracy in phase errors may lead to flow re-laminarization. Therefore, we must ask how *long-time integration* relates to the formal order of accuracy of a numerical scheme, and what is the corresponding computational cost? To this end, let us consider the convection of a waveform at a constant speed. Let us now assume that there are $N^{(k)}$ grid points required per wavelength to reduce the error to a level ϵ, where k denotes the formal order of the scheme. In addition, let us assume that we integrate for M *time periods*. We can neglect temporal errors $\mathcal{O}(\Delta t)^J$ (where J is the order of the time integration) by assuming a sufficiently small time step Δt. We wish to estimate the phase error in this simulation for second- $N^{(2)}$, fourth- $N^{(4)}$, and sixth- $N^{(6)}$ order finite difference schemes. The complete analysis is presented in ([5]), and here we present the results for the computational work. In figure 3 we compare the efficiency of these three different discretizations for the *same phase error* by plotting the computational work required to maintain an "engineering" accuracy of 10% versus the number of time periods for the integration. This comparison favors the fourth-order scheme for short times ($M \propto \mathcal{O}(1)$) over both the second-order and the sixth-order schemes. However, for long-time integration ($M \propto \mathcal{O}(100)$), even for this engineering accuracy of 10%, the sixth-order scheme is superior as the corresponding operation count $W^{(6)}$ is about 6 times lower than the operation count of the second-order scheme $W^{(2)}$, and half the work of the fourth-order scheme $W^{(4)}$. For an accuracy of 1% in the solution of this convection problem, the sixth-order scheme is superior even for short-time integration.

High-order accuracy, however, does not automatically imply a resolved and thus accurate DNS or LES. In particular, spectral-based methods tend to behave differently when the number of grid points or modes is insufficient. For example, they tend to be more unstable, lead to over-prediction of amplitudes, and could even result in erroneous unsteady flow at subcritical conditions. This is the primary topic that we focus on in the present paper.

Specifically, we first review some key developments in extending spectral methods to unstructured grids for both incompressible and compressible flows. We then discuss in some detail the effect of under-

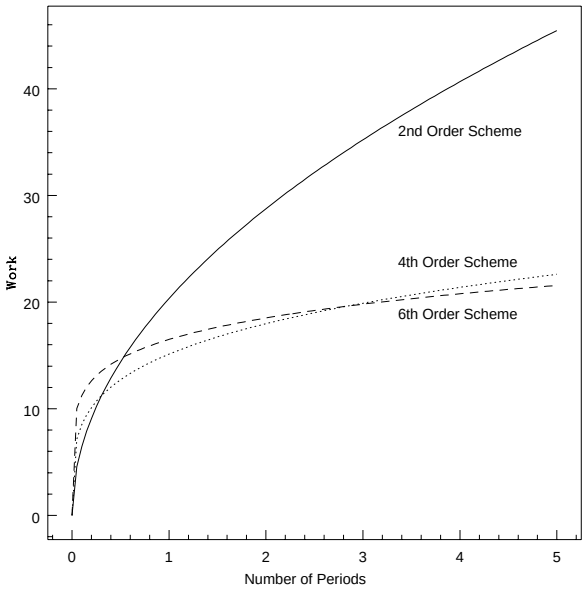

Figure 3. Computational work (number of floating-point operations) required to integrate a linear advection equation for M periods while maintaining a cumulative phase error of 10%.

resolving the discretization of nonlinear terms and how dealising can be handled on non-uniform grids presenting both one-dimensional examples but also full DNS of turbulent flow that may suffer from aliasing. We then proceed with several examples of internal and external flows and document diagnostics that can be employed to detect erroneous physics. We also include simulations of some turbulent flows which, although clearly under-resolved, lead to useful results in agreement with the experiments. Finally, we conclude with a perspective on simulating turbulence in fully three-dimensional domains where both numerical uncertainty and physical uncertainty are adequately characterized.

2. Spectral Methods on Unstructured Grids

There have been more than fifteen years of developments in extending spectral methods to complex-geometry domains ([5]), starting with the pioneering work of ([6]), who developed spectral methods in the context of a multi-element variational formulation similar to finite element methods. This allowed the use of spectral (Chebyshev or Legendre) expansions as trial basis in general quadrilateral subdomains. Conti-

nuity of data and unknowns across subdomains is ensured via appropriate construction of the trial basis similar to finite element methods for second-order elliptic problems. Such methods were used to produce the first spectral DNS of turbulence in complex-geometry domain, flow over riblets, in ([7]). An extension to non-conforming discretizations for turbulent flows, which are more appropriate for local refinement, was presented in ([8]).

The new generation of spectral methods developed recently is more appropriate for discretizations on unstructured grids consisting of triangles and tetrahedra, similar to grids used in aerodynamics ([9, 10]). In many simulations, however, it is more efficient to employ hybrid discretizations, i.e. discretizations using a combination of structured and unstructured subdomains. This is a recent trend in computational mechanics involving complex three-dimensional computational domains ([11, 12]). Such an approach combines the simplicity and convenience of structured domains with the geometric flexibility of an unstructured discretization. In two-dimensions, hybrid discretization simply implies the use of triangular and rectangular subdomains, however in three-dimensions the hybrid strategy is more complex requiring the use of hexahedra, prisms, pyramids and tetrahedra.

We have developed a unified description in dealing with elements of different shape in two- and three-dimensions. This unified approach generates polynomial expansions which can be expressed in terms of a *generalized* product of the form

$$\phi_{pqr}(x, y, z) = \phi^a_p(x)\phi^b_{pq}(y)\phi^c_{pqr}(z).$$

Here we have used the Cartesian co-ordinates x, y and z but, in general, they can be any set of co-ordinates defining a specified region. The standard tensor product is simply a degenerate case of this product, where the second and third functions are only dependent on one index. The primary motivation in developing an expansion of this form is computational efficiency. Such expansions can be evaluated in three-dimensions in $O(P^4)$ operations as compared to $O(P^6)$ operations with non-tensor products (where P is the number of spectral modes per direction).

2.1 Local Co-ordinate Systems

We start by defining a convenient set of local co-ordinates upon which we can construct the expansions. Unlike the barycentric co-ordinates, which are typically applied to unstructured domains in linear finite elements, we define a set of *collapsed Cartesian* co-ordinates in non-rectangular domains. These co-ordinates will form the foundation of the polynomial expansions. The advantage of this system is that every do-

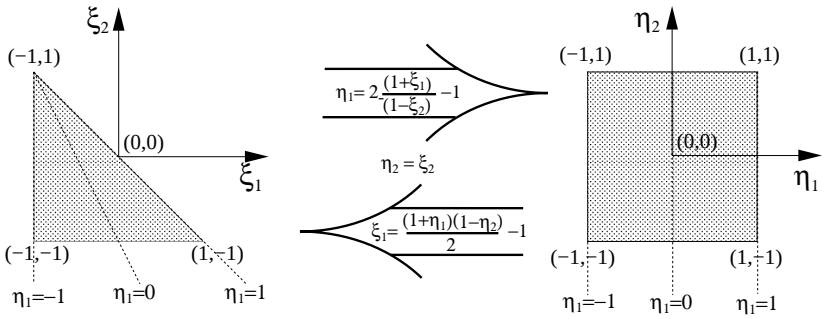

Figure 4. Triangle to rectangle transformation

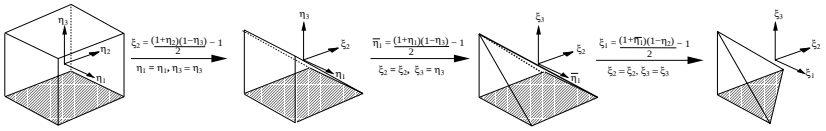

Figure 5. Hexahedron to tetrahedron transformation

main can be bounded by constant limits of the new local co-ordinates; accordingly operations such as integration and differentiation can be performed using standard one-dimensional techniques.

The new co-ordinate systems are based upon the transformation of a triangular region to a rectangular domain (and vice versa) as shown in figure 4. The main effect of the transformation is to map the vertical lines in the rectangular domain (i.e. lines of constant η_1) onto lines radiating out of the point $(\xi_1 = -1, \xi_2 = 1)$ in the triangular domain. The triangular region can now be described using the "ray" co-ordinate (η_1) and the standard horizontal co-ordinate $(\xi_2 = \eta_2)$. The triangular domain is therefore defined by $(-1 \leq \eta_1, \eta_2 \leq 1)$ rather than the Cartesian description $(-1 \leq \xi_1, \xi_2;\ \ \xi_1 + \xi_2 \leq 0)$ where the upper bound couples the two co-ordinates. The "ray" co-ordinate (η_1) is multi-valued at $(\xi_1 = -1, \xi_2 = 1)$. Nevertheless, we note that the use of singular co-ordinate systems is very common, arising in both cylindrical and spherical co-ordinate systems.

As illustrated in figure 5, the same transformation can be repeatedly applied to generate new co-ordinate systems in three-dimensions. Here, we start from the bi-unit hexahedral domain and apply the triangle to rectangle transformation in the vertical plane to generate a prismatic region. The transformation is then used in the second vertical plane to generate the pyramidic region. Finally, the rectangle to triangle trans-

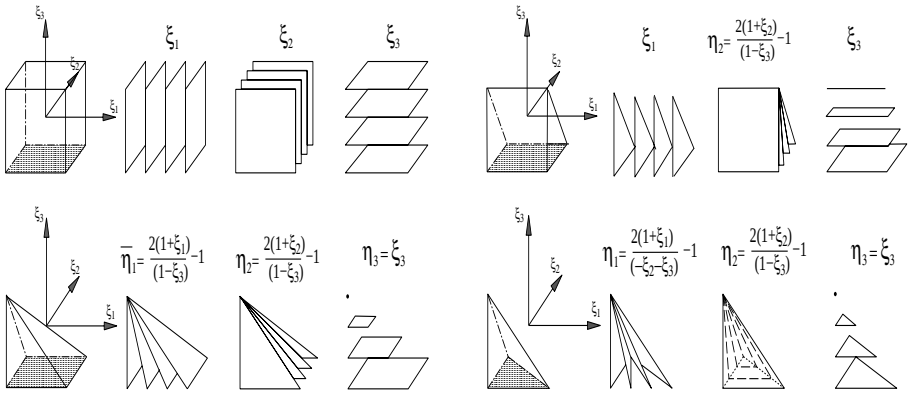

Figure 6. The local coordinate systems used in each of the hybrid elements and the planes described by fixing each local co-ordinate.

formation is applied to every square cross section parallel to the base of the pyramidic region to arrive at the tetrahedral domain.

By determining the hexahedral co-ordinates (η_1, η_2, η_3) in terms of the Cartesian co-ordinates of the tetrahedral region (ξ_1, ξ_2, ξ_3) we can generate a new co-ordinate system for the tetrahedron. This new system and the planes described by fixing the local co-ordinates are shown in figure 6. Also shown are the new systems for the intermediate domains which are generated in the same fashion. Here we have assumed that the local Cartesian co-ordinates for every domain are (ξ_1, ξ_2, ξ_3).

2.2 Hierarchical Expansions

For each of the hybrid domains we can develop a polynomial expansion based upon the local co-ordinate system derived in section 2.1. These expansions will be polynomials in terms of the local co-ordinates as well as the Cartesian co-ordinates (ξ_1, ξ_2, ξ_3). This is a significant property as primary operations such as integration and differentiation can be performed with respect to the local co-ordinates but the expansion may still be considered as a polynomial expansion in terms of the Cartesian system.

We shall initially consider expansions which are orthogonal in the Legendre inner product. We define three principle functions $\phi_i^a(z), \phi_{ij}^b(z)$ and $\phi_{ijk}^c(z)$, in terms of the Jacobi polynomial, $P_p^{\alpha,\beta}(z)$, as:

$$\phi_i^a(z) = P_i^{0,0}(z), \qquad \phi_{ij}^b(z) = \left(\tfrac{1-z}{2}\right)^i P_j^{2i+1,0}(z),$$

$$\phi_{ijk}^c(z) = \left(\tfrac{1-z}{2}\right)^{i+j} P_k^{2i+2j+2,0}(z).$$

Using these functions we can construct the orthogonal polynomial expansions:

$$\text{Hexahedral expansion: } \phi_{pqr}(\xi_1,\xi_2,\xi_3) = \phi^a_p(\xi_1)\phi^a_q(\xi_2)\phi^a_r(\xi_3)$$

$$\text{Prismatic expansion: } \phi_{pqr}(\xi_1,\xi_2,\xi_3) = \phi^a_p(\xi_1)\phi^a_q(\eta_2)\phi^b_{qr}(\xi_3)$$

$$\text{Pyramidic expansion: } \phi_{pqr}(\xi_1,\xi_2,\xi_3) = \phi^a_p(\overline{\eta_1})\phi^a_q(\eta_2)\phi^c_{pqr}(\eta_3)$$

$$\text{Tetrahedral expansion: } \phi_{pqr}(\xi_1,\xi_2,\xi_3) = \phi^a_p(\eta_1)\phi^b_{pq}(\eta_2)\phi^c_{pqr}(\eta_3)$$

where,

$$\eta_1 = \frac{2(1+\xi_1)}{(-\xi_2-\xi_3)} - 1, \quad \overline{\eta_1} = \frac{2(1+\xi_1)}{(1-\xi_3)} - 1, \quad \eta_2 = \frac{2(1+\xi_2)}{(1-\xi_3)} - 1, \quad \eta_3 = \xi_3,$$

are the local co-ordinates illustrated in figure 6.

The hexahedral expansion is simply a standard tensor product of Legendre polynomials (since $P^{0,0}_p(z) = L_p(z)$). In the other expansions the introduction of the degenerate local co-ordinate systems is linked to the use of the more unusual functions $\phi^b_{ij}(z)$ and $\phi^c_{ijk}(z)$. These functions both contain factors of the form $\left(\frac{1-z}{2}\right)^p$ which is necessary to keep the expansion as a polynomial of the Cartesian co-ordinates (ξ_1,ξ_2,ξ_3). For example, the co-ordinate η_2 in the prismatic expansion necessitates the use of the function $\phi^b_{qr}(\xi_3)$ which introduces a factor of $\left(\frac{1-\xi_3}{2}\right)^q$. The product of this factor with $\phi^a_q(\eta_2)$ is a polynomial function in ξ_2 and ξ_3. Since the remaining part of the prismatic expansion, $\phi^a_p(\xi_1)$, is already in terms of a Cartesian co-ordinate the whole expansion is a polynomial in terms of the Cartesian system.

The polynomial space, in Cartesian co-ordinates, for each expansion is:

$$\mathcal{P} = \text{Span}\{\xi_1^p\ \xi_2^q\ \xi_3^r\} \tag{1}$$

where pqr for each domain is

$$\begin{array}{lccc} \text{Hexahedron} & 0 \le p \le P_1 & 0 \le q \le P_2 & 0 \le r \le P_3 \\ \text{Prism} & 0 \le p \le P_1 & 0 \le q \le P_2 & 0 \le q+r \le P_3 \\ \text{Pyramidic} & 0 \le p \le P_1 & 0 \le q \le P_2 & 0 \le p+q+r \le P_3 \\ \text{Tetrahedron} & 0 \le p \le P_1 & 0 \le p+q \le P_2 & 0 \le p+q+r \le P_3. \end{array} \tag{2}$$

The range of the p, q and r indices indicate how the expansions should be expanded to generate a complete polynomial space. We note that if $P_1 = P_2 = P_3$ then the tetrahedral and pyramidic expansions span the same space and are in a subspace of the prismatic expansion which is in turn a subspace of the hexahedral expansion.

2.3 Galerkin and Discontinuous Galerkin Projections

To obtain a system of nonlinear algebraic equations, we employ different projections and time integration algorithms. In particular, for *incompressible flows* we use a linear Galerkin projection in conjunction with the high-order fractional stepping scheme described in ([13, 14]). For *compressible flows*, we use a discontinuous Galerkin projection with multi-step explicit time integration ([15]).

We describe both approaches next with more emphasis on the latter which is a more recent development.

Incompressible Flows. The standard approach in treating the incompressible Navier-Stokes equations is to combine a semi-implicit scheme with a fractional procedure ([5]) following the Eulerian description. Here we consider a more recent development that takes advantage of semi-Lagrangian treatment for advection. This allows for large size time steps in simulations of turbulence, where at high Reynolds number the temporal scales are largely over-resolved. Following ([16]) we consider the Navier-Stokes equations in Lagrangian form

$$\frac{d\mathbf{u}}{dt} = -\nabla p + \nu \nabla^2 \mathbf{u}, \tag{3}$$

$$\nabla \cdot \mathbf{u} = \mathbf{0}, \tag{4}$$

where d/dt denotes a Lagrangian derivative. We employ a stiffly-stable second-order scheme to discretize the time derivative:

$$\frac{\frac{3}{2}u^{n+1} - 2u_d^n + \frac{1}{2}u_d^{n-1}}{\Delta t} = (-\nabla p + \nu \nabla^2 u)^{n+1}, \tag{5}$$

where u_d^n is the velocity u at the departure point x_d^n at time level t^n, and u_d^{n-1} is the velocity at the departure point x_d^{n-1} at time level t^{n-1}. The departure point x_d^n is obtained by solving

$$\frac{dx}{dt} = u^{n+1/2}(x,t), \quad x(t^{n+1}) = x_a$$

and also

$$u^{n+1/2} = 3/2u^n - 1/2u^{n-1}.$$

The point x_d^{n-1} is obtained by solving

$$\frac{dx}{dt} = u^n(x,t), \quad x(t^{n+1}) = x_a.$$

By using the above characteristic equations, the resulting scheme is second-order accurate in time.

Specifically, for computational convenience we use the following three substeps to solve equation (5)

$$\frac{\hat{u} - 2u_d^n + \frac{1}{2}u_d^{n-1}}{\Delta t} = 0, \tag{6}$$

$$\frac{\hat{\hat{u}} - \hat{u}}{\Delta t} = -\nabla p^{n+1}, \tag{7}$$

$$\frac{\frac{3}{2}u^{n+1} - \hat{\hat{u}}}{\Delta t} = \nu \nabla^2 u^{n+1}. \tag{8}$$

The discrete divergence-free condition results in a consistent Poisson equation for the pressure, i.e.

$$\nabla^2 p^{n+1} = \frac{1}{\Delta t} \nabla \cdot \hat{u},$$

with accurate pressure boundary conditions of the form ([5])

$$\frac{\partial p}{\partial n} = -\nu \cdot [\hat{u} + \nabla \times \omega^{n+1}],$$

where n is the unit normal, and ω is the vorticity ([14]).

The semi-Lagrangian approach is typically more expensive than the corresponding Eulerian approach, but in practice the larger size of time step allowed in the former leads to more efficient simulations. This was demonstrated for two- and three-dimensional flows in ([16]).

With regards to *spatial discretization*, in order to enforce the required C^0 continuity, the orthogonal expansion is modified by decomposing the expansion into an *interior* and *boundary contribution*. This results in partially sacrificing orthogonality. The interior modes (or bubble functions) are defined to be zero on the boundary of the local domain. The completeness of the expansion is then ensured by adding boundary modes which consist of

- Vertex, Edge, and Face contributions.

The *vertex modes* have unit value at one vertex and decay to zero at all other vertices; *edge modes* have local support along one edge and are zero on all other edges and vertices, and *face modes* have local support on one face and are zero on all other faces, edges and vertices. C^0 continuity between elements can then be enforced by matching similar shaped boundary modes. The local co-ordinate systems do impose some

restrictions on the orientation in which triangular faces may connect. However, it has been shown in ([10]) that a C^0 tetrahedral expansion can be constructed for any tetrahedral mesh. A similar strategy could be applied to a hybrid discretization.

Compressible Flows. We consider the non-dimensionalized compressible Navier-Stokes equations, which we write in compact form as

$$\vec{U}_t + \nabla \cdot \mathbf{F} = Re_\infty^{-1} \nabla \cdot \mathbf{F}^\nu \tag{9}$$

where $\mathbf{F}$ and $\mathbf{F}^\nu$ correspond to inviscid and viscous flux contributions, respectively. Here the vector $\vec{U} = [\rho, \rho u, \rho v, \rho w, E]^t$ with (u, v, w) the local fluid velocity, ρ the fluid density, and E the total internal energy. Splitting the Navier-Stokes operator in this form allows for the separate treatment of the inviscid and viscous contributions, which in general exhibit different mathematical properties. In the following, we review briefly the discontinuous Galerkin formulations employed in the proposed method. A systematic analysis of the advection operator was presented in ([17]), where a mixed formulation was used to treat the diffusion terms. No flux limiters are necessary as has been found before in ([18]) and has been justified theoretically in ([19]).

We first use a linear two-dimensional **advection equation** of a conserved quantity u in a region Ω, in order to illustrate the treatment of inviscid contributions:

$$\frac{\partial u}{\partial t} + \nabla \cdot \mathbf{F}(u) = 0, \tag{10}$$

where $\mathbf{F}(u) = (f(u), g(u), h(u))$ is the *flux* vector which defines the transport of $u(\mathbf{x}, t)$. We start with the variational statement of the standard Galerkin formulation of (10) by multiplying by a test function v and integrating by parts

$$\int_\Omega \frac{\partial u}{\partial t} v \, dx + \int_{\partial\Omega} v \, \hat{n} \cdot \mathbf{F}(u) \, ds - \int_\Omega \nabla v \cdot \mathbf{F}(u) \, dx = 0. \tag{11}$$

The solution $u \in \mathcal{X}$ (approximation space) satisfies this equation for all $v \in \mathcal{V}$ (test space). The requirement that $\mathcal{X}$ consist of continuous functions naturally leads to a basis consisting of functions with overlapping support, which implies equation (11) becomes a banded matrix equation. Solving the corresponding large system is not a trivial task for parallel implementations, and therefore a different type of formulation is desirable.

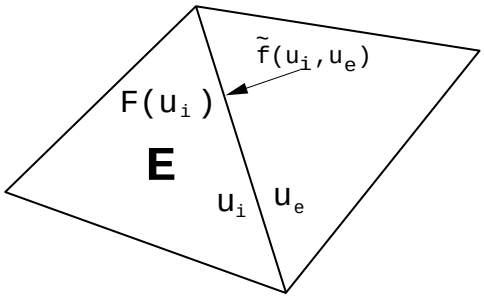

Figure 7. Interface conditions between two adjacent triangles.

Another consideration from the point of view of advection is that continuous function spaces are not the natural place to pose the problem. Mathematically, hyperbolic problems of this type tend to have solutions in spaces of bounded variation. In physical problems, the best one can hope for in practice is that solutions will be piecewise continuous, that is, be smooth in regions separated by discontinuities (shocks). An additional consideration is that the formulation presented next preserves automatically conservativity in the element-wise sense.

These considerations suggest immediately a formulation where $\mathcal{X}$ may contain discontinuous functions. The discrete space $\mathcal{X}^\delta$ contains polynomials within each "element," but zero outside the element. Here the "element" is, for example, an individual triangular region T_i in the computational mesh applied to the problem. Thus the computational domain $\Omega = \bigcup_i T_i$, and T_i, T_j overlap only on edges.

Contending with the discontinuities requires a somewhat different approach to the variational formulation. Each element (E) is treated separately, giving a variational statement (after integrating by parts once more):

$$\frac{\partial}{\partial t}(u, v)_E + \int_{\partial T_E} v(\tilde{f}(u_i, u_e) - \boldsymbol{f}(u_i))\cdot\mathbf{n}\, ds + (\nabla \cdot \boldsymbol{f}(u), v)_E = 0, \quad (12)$$

where $\boldsymbol{f}(u_i)$ is the flux of the interior values. Computations on each element are performed separately, and the connection between elements is a result of the way boundary conditions are applied. Here, boundary conditions are enforced via the numerical surface flux $\tilde{f}(u_i, u_e)$ that appears in equation (12). Because this value is computed at the boundary between adjacent elements, it may be computed from the value of u given at either element. These two possible values are denoted here as u_i in the interior of the element under consideration and and u_e in the exterior (see figure 7). Upwinding considerations dictate how this flux

is computed. In the more complicated case of a hyperbolic system of equations, an approximate Riemann solver should be used to compute a value of f, g, h (in three-dimensions) based on u_i and u_e. Specifically, we compute the flux $\tilde{f}(u_i, u_e)$ using upwinding, i.e.

$$\tilde{f}(u) = R\Lambda^+ L u_i + R\Lambda^- L u_e$$

where A (the Jacobian matrix of F) is written in terms of the left and right eigenvectors, i.e. $A = R\Lambda L$ with Λ containing the corresponding eigenvalues in the diagonal; also, $\Lambda^{\pm} = (\Lambda \pm |\Lambda|)/2$. Alternatively, we can use a standard Lax-Friedrichs flux

$$\tilde{f}(u) = \frac{1}{2}(f(u_e) + f(u_i)) - \frac{1}{2}R|\Lambda|L(u_e - u_i).$$

This last form is what is used in the airfoil example presented in section 4.

Next, we consider as a model problem the **parabolic equation** with variable coefficient ν to demonstrate the treatment of the viscous contributions:

$$u_t = \nabla \cdot (\nu \nabla u) + f, \quad \text{in } \Omega, \quad u \in L^2(\Omega)$$
$$u = g(\mathbf{x}, t), \quad \text{on } \partial\Omega$$

We then introduce the flux variable

$$\mathbf{q} = -\nu \nabla u$$

with $\mathbf{q}(\mathbf{x}, t) \in \mathbf{L}^2(\Omega)$, and re-write the parabolic equation

$$u_t = -\nabla \cdot \mathbf{q} + f, \quad \text{in } \Omega$$
$$1/\nu \mathbf{q} = -\nabla u, \quad \text{in } \Omega$$
$$u = g(\mathbf{x}, t), \quad \text{on } \partial\Omega.$$

The weak formulation of the problem is then as follows: Find $(\mathbf{q}, u) \in \mathbf{L^2(\Omega)} \times L^2(\Omega)$ such that

$$(u_t, w)_E = (\mathbf{q}, \nabla w)_E - < w, \mathbf{q_b} \cdot \mathbf{n} >_E + (f, w)_E, \quad \forall w \in L^2(\Omega)$$
$$1/\nu(\mathbf{q}^m, \mathbf{v})_E = (u, \nabla \cdot \mathbf{v})_E - < u_b, \mathbf{v} \cdot \mathbf{n} >_E, \quad \forall \mathbf{v} \in \mathbf{L^2(\Omega)}$$
$$u = g(\mathbf{x}, t), \quad \text{on } \partial\Omega$$

where the parentheses denote standard inner product in an element (E) and the angle brackets denote boundary terms on each element, with $\mathbf{n}$ denoting the unit outwards normal. The surface terms contain weighted

boundary values of v_b, q_b, which can be chosen as the arithmetic mean of values from the two sides of the boundary, i.e.

$$v_b = (v_i + v_e)/2,$$

and

$$q_b = (q_i + q_e)/2.$$

The consequences of choosing different numerical fluxes with regards to stability and accuracy have been investigated in ([20]).

By integrating by parts once more, we obtain an equivalent formulation which is easier to implement, and it is actually used in the computer code. The new variational problem is

$$(u_t, w)_E = (-\nabla \cdot \mathbf{q}, w)_E - < w, (\mathbf{q_b} - \mathbf{q_i}) \cdot \mathbf{n} >_E + (f, w)_E, \quad \forall w \in L^2(\Omega)$$

$$1/\nu(\mathbf{q}, \mathbf{v})_E = (-\nabla u, \mathbf{v})_E - < u_b - u_i, \mathbf{v} \cdot \mathbf{n} >_E, \quad \forall \mathbf{v} \in \mathbf{L^2(\Omega)}$$

$$u = g(\mathbf{x}, t), \quad \text{in } \partial\Omega$$

where the subscript (i) denotes contributions evaluated at the interior side of the boundary. We integrate the above system *explicitly* in time and employ the orthogonal Jacobi polynomials as trial and test basis.

3. Nonlinearities and Dealising

In spectral methods the quadratic nonlinearities in the incompressible Navier-Stokes equations or the cubic nonlinearities in the compressible Navier-Stokes are computed in the physical space. Specifically, the fields (velocity, pressure, energy) are first transformed into physical space and subsequently the products are obtained at all quadrature points in a collocation fashion. Another transform is then performed to bring the results back to modal space. More specifically, when the number of quadrature points Q is the same as the number of modes in the spectral expansion P we have a true collocation method, otherwise for $Q > P$ we have a super-collocation method.

The form in which we write the nonlinear terms, that is,

- in convective (flux), or
- skew-symmetric, or
- rotation form

is also important. In spectral DNS of boundary layers and channel flows, the rotation form is usually preferred over the convective form as it semi-conserves energy (in the inviscid limit). This, typically, makes it more

stable, especially for the long-time integration required in DNS. In addition, it is more economical as it requires the evaluation of only six derivatives whereas the convective form requires nine derivative evaluations. The skew-symmetric form was found to be more "forgiving" in aliasing errors in under-resolved simulations of homogeneous turbulence compared to the rotation form. This is also true for finite difference methods; see the article of ([21]) in this volume where it is shown that skew-symmetry leads to symmetry preservation and enhanced stability. However, the skew-symmetric form requires the evaluation of 18 derivatives which is computationally more expensive.

There is not sufficient experience yet with spectral/hp element DNS to conclusively suggest one form or the other although there is some consensus that the convective form is quite accurate and leads to stable discretizations. A comparison of the different forms (convective, flux, and skew-symmetric) was performed in ([22]) for a constant advection velocity as well as for a spatially varying divergent-free velocity $(u, v) = (-\sin x_2 \cos x_1, \sin x_1 \cos x_2)$. The discretization was based on a nodal Gauss-Lobatto-Legendre basis. The result was that for the constant advection velocity all forms were the same in that they produced identical eigenspectrum with all imaginary eigenvalues. However, for the variable advection velocity, only the skew-symmetric form gave imaginary eigenvalues with the convective and conservative form producing complex eigenvalues with positive real parts. For purely convection equations, these spurious positive values may lead to instabilities if explicit time stepping is used. However, for Navier-Stokes computations at modest Reynolds number no such instabilities have been observed, presumably due to the stabilizing role of the viscous terms. Although the skew-symmetric form is usually considered the most accurate, problems may also be encountered with this form for Dirichlet and inflow/outflow conditions. This is presented in some detail in ([5]) using a numerical experiment performed by ([23]).

Finally, errors may be caused by insufficient quadrature used in the spectral/hp element discretization of the nonlinear terms, especially in complex-geometry flows. These errors can be eliminated effectively by employing over-integration, i.e. integrating the nonlinear terms in the variational statement with higher order quadrature than the one employed for the linear contributions, e.g. pressure and viscous terms. We will examine this issue in some detail next.

3.1 Accuracy, Stability and Over-Integration

To understand the ramifications of under-integration of nonlinear terms, we perform the following test:

1 Consider a single element in the space interval $[-1, 1]$ containing $P = 16$ Jacobi modes.

2 Initialize all the modal coefficients to one.

3 Evaluate the modal representation on a set of Q quadrature points.

4 Square (in a pointwise fashion) the values at the quadrature points.

5 Pre-multiply the set of points (as a vector) by the collocation derivative matrix of the appropriate size (rank $Q \times Q$).

6 Project back to modal coefficients by discrete inner products using Gaussian integration.

The procedure above mimics the "physical space" or pseudo-spectral evaluation of the term $\frac{\partial u^2}{\partial x}$ commonly used in spectral methods for evaluating nonlinear terms. This test was chosen because even in its simplicity it models the order of nonlinearity that occurs in the solution of the incompressible Navier-Stokes equations. All modes are set to *one* to mimic a case in which an element has under-resolved or marginally resolved the solution within the element. In the test above, the only unspecified parameter is the number of quadrature points Q to be used. In using Gauss-Lobattto points, the value of Q is taken to be one more than the number of modes P (in this case then $P = 16$ and $Q = 17$) ([24]), but this value is appropriate for the inner products corresponding to linear terms. For quadratic or cubic nonlinearities more quadrature points are required. The ramifications of under-integration of this form are shown in figure 8. The figure on the left was obtained for quadratic nonlinearity ($\frac{\partial}{\partial x}u^2$) and the figure on the right was obtained for a cubic nonlinearity ($\frac{\partial}{\partial x}u^3$). The difference in the modal coefficients at the conclusion of the algorithm above for different values of Q is provided. We observe that for the quadratic nonlinearity, once $\frac{3}{2}P$ quadrature points are used, the differences in the modal values do not change. Similarly for the cubic nonlinearity, once $2P$ quadrature points are used the differences in the modal values do not change.

In order to appreciate the effect of under-integration in the context of a numerical solution, we consider the inviscid Burgers equation, which we discretize using the discontinuous Galerkin method. The initial condition is $-\sin(\pi x)$, and five equally spaced elements spanning $[-1, 1]$

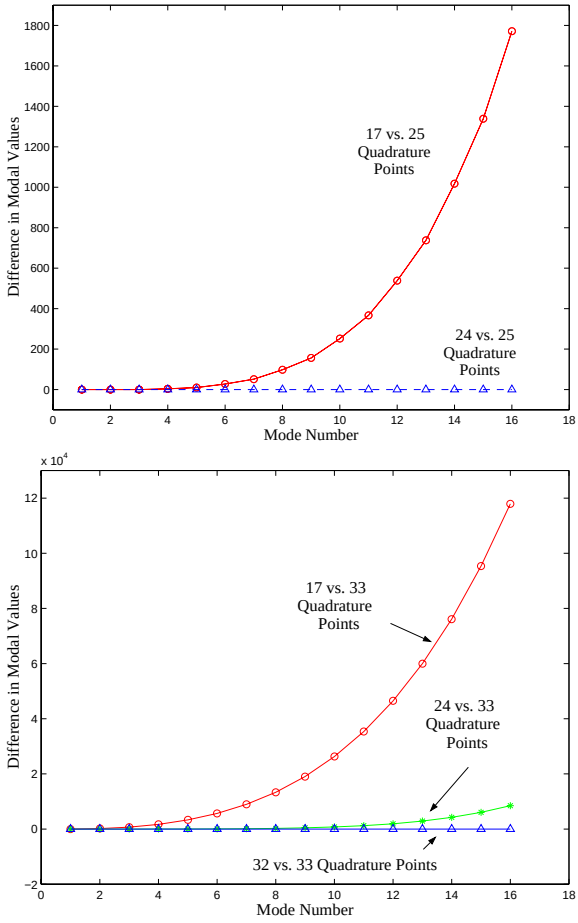

Figure 8. Comparison of the difference in modal coefficients when different numbers of quadrature points are used. Quadratic nonlinearity is shown on the left and cubic nonlinearity is shown on the right.

were used, each one having $P = 16$ modes. In figure 9, we plot the L_2 norm of the solution versus the number of quadrature points used for numerical integration. When using $Q = 17, 19$ and $Q = 21$ points, the solution is unstable (denoted by the blue *). Once the number of quadrature points reaches $Q = 24$ ($\frac{3}{2}P$ where P is the number of modes), the L_2 norm of the solution does not change.

We can analyze this behavior by examining the energy in the modes (denoted by the square of the modal values) within the element that contains the jump in the inviscid Burgers solution. The modes were extracted at time $T = 0.35$, after the shock has formed (at time $\frac{1}{\pi}$) and

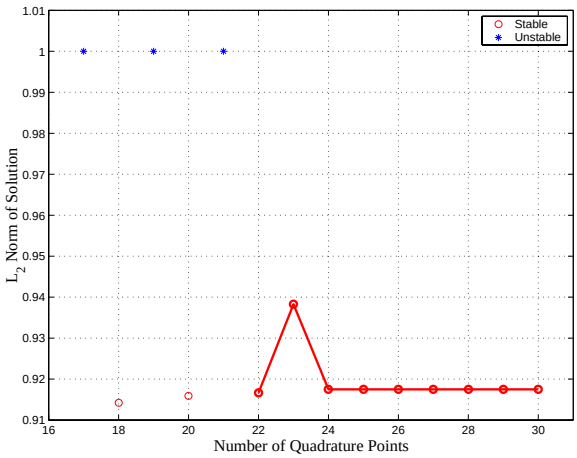

Figure 9. Solution of the inviscid Burgers equation evaluated at $T = 0.5$. Five equal spaced elements were used with 16 modes in each element. On the ordinate we plot the L_2 norm of the solution, and on the abscissa we plot the number of quadrature points used for numerical integration. Unstable solutions are denoted by blue *. Observe that after $Q = 24$ points, the L_2 norm of the solution does not change.

prior to the solution becoming unstable. In figure 10, we plot the square of the modal coefficients versus the mode number. Due to the symmetry of the element placement, only even number modes were excited.

This case corresponds to $Q = 17$ quadrature points being used, which from the figure 9, we know will become unstable by time $T = 0.5$. If a $\frac{3}{2}P$ rule is used, yielding $Q = 24$ points, the solution is stable, and the energy is much less than when the non-linear terms are under-integrated. This plot shows vividly the effects of aliasing when under-integration of the non-linear terms is performed.

An alternative way of handling instabilities associated with nonlinearities in hyperbolic conservation laws is through *monotonicity preserving schemes*. An approach suitable for high-order methods has been developed by ([25]) and was employed in large-eddy simulations in ([26]). It involves the addition of a *second-order convolution kernel* that acts on each mode separately and controls the high modes suppressing preferentially erroneous high-frequency oscillations. This type of nonlinear kernel has been termed as spectral vanishing viscosity (SVV). As an example, the inviscid Burgers equation with the SVV term added is

$$\frac{\partial u}{\partial t} + \frac{1}{2}\frac{\partial u^2}{\partial x} = \epsilon \frac{\partial}{\partial x}(Q_k * \frac{\partial u}{\partial x}). \tag{13}$$

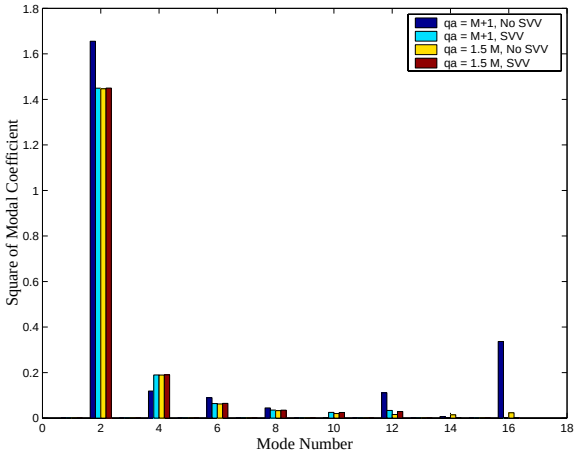

Figure 10. Modal coefficients of the inviscid Burgers solution before blow up. Both over-integration and SVV lead to a stable solution unlike the collocation approach.

Here $\epsilon \propto 1/P$, i.e. it is inversely proportional to the number of modes, and Q_k is a smooth kernel that facilitates a transition between the controlled high modes and the uncontrolled and more energetic low modes. It is given by

$$\hat{Q}_k = e^{-\frac{(k-P)^2}{(k-P_c)^2}}, \quad k > P_c.$$

The cut-off wave number P_c scales as $P_c \approx \sqrt{P}$, asymptotically for P large. Although the above can be considered as a viscosity regularization procedure there is a significant difference as has been demonstrated in ([27]), see also ([26]). The parameters ϵ and Q_k are chosen so that monotonicity is preserved while the spectral accuracy in the solution is also maintained. In figure 10 we demonstrate how the addition of SVV leads to effectively the same results as over-integration but operating with a collocation discretization, i.e. $Q = P + 1$. The modal coefficients of the inviscid Burgers solution converge monotonically to zero leading to a stable simulation unlike the collocation untreated simulation.

3.2 Transition and Turbulence in a Triangular Duct

We demonstrate next the effect of under-integration and associated aliasing errors by simulating transition to turbulence of incompressible flow in a duct with its cross-section being an equilateral triangle. The laminar fully-developed solution is known analytically. We introduce some random disturbances in the flow and we integrate in time until

these disturbances start decaying or growing in time. All simulations were performed in the domain shown in figure 11 with the cross-section discretized using one triangular element only and 16 Fourier modes (32 collocation points) in the streamwise (homogeneous) direction. The Reynolds number is defined as $Re = UD_e/\nu$ where U is the average velocity and D_e is the equivalent (hydraulic) diameter. For $Re \leq 500$ all disturbances decay but for $Re = 1250$ the flow goes through transition and a turbulent state is sustained.

We have performed three simulations at $Re = 1250$ corresponding to three different combinations of polynomial and quadrature order. In the first one, shown in 11(a), we consider the case where $Q = P + 1$, where $P = 16$. The forces on the three walls of the duct are plotted as a function of time. From symmetry considerations, we expect that the statistical averages of the three forces are identical but obviously the symmetry is not preserved here. In figure 11(b) we plot the forces for the case with $Q = 2P$, and in figure 11(c) the case with $Q = 3P/2$. We have verified that in both cases the same statistical force average is obtained, consistent with the analysis presented above for handling under-integration induced errors.

Based on the above analysis and result as well as other similar results, we can state the following semi-empirical rule:

Dealising Rule: For quadratic nonlinearities employing super-collocation with $3/2\,P$ grid (quadrature) points per direction, where P is the polynomial order per direction, followed by a Galerkin projection leads to a dealiased turbulence simulation on non-uniform meshes.

4. Under-Resolution and Diagnostics

Spectral and spectral/*hp* element methods behave, in general, differently than low-order methods in under-resolved simulations. Spectral discretizations are more susceptible to numerical instabilities than other low-order discretizations. This could be frustrating for the users who seek robustness but it is actually safe-guarding against erroneous answers, as typically spectral codes blow up in seriously under-resolved simulations. In under-resolved spectral discretizations there are many more wiggles, and therefore it is easier to detect suspicious simulations before resorting to more rigorous error estimation. Also, spectral discretizations typically suffer from little numerical dissipation unlike finite-difference methods, which introduce an erroneous numerical viscosity in low resolution discretizations. This effectively lowers the nominal Reynolds number of the simulated flow and leads to stable simulations

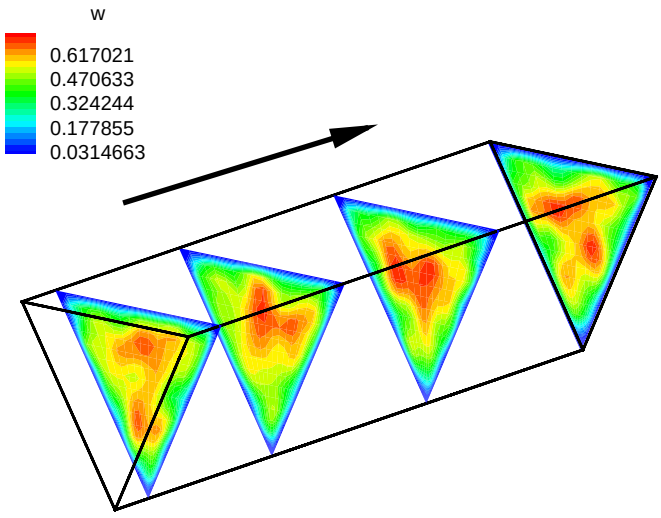

Figure 11. Duct flow domain: The cross-section is an equilateral triangle and the streamwise length is three times the triangle edge. Shown is a snapshot of streamwise velocity contours at $Re = 1250$.

but with the incorrect physics. This is not true in spectral/hp discretizations where the nominal Reynolds number is also the effective Reynolds number. However, such behavior in conjunction also with the presence of high-wave number wiggles, may sometimes be the source of erroneous instabilities in under-resolved spectral flow simulations. For example, the resulting velocity profiles may not be monotonic and thus are susceptible to inviscid type instabilities, which in turn promote transition from steady to unsteady flow or transition to higher bifurcations and eventually turbulence. For open unsteady flows, the amplitude of the oscillation in an under-resolved simulation is usually over-predicted.

In the following, we present a few examples of under-resolved flows that affect both transition to turbulence as well as turbulence statistics. We also include a case of transient compressible flow past an airfoil where under-resolution may seriously affect the lift. However, as we will see not all results from under-resolved simulations are inaccurate. Some flows exhibit low-dimensionality and the energetics of low modes dominate so

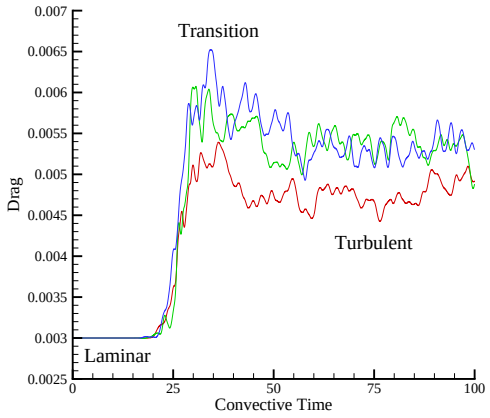

(a)

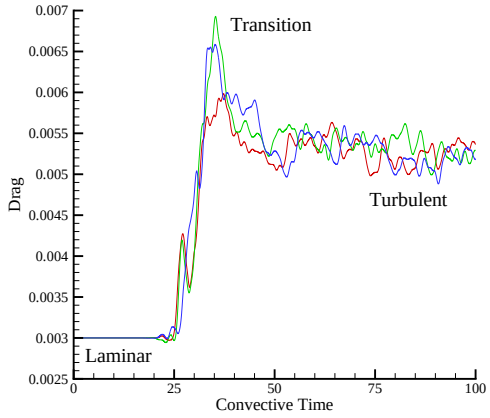

(b)

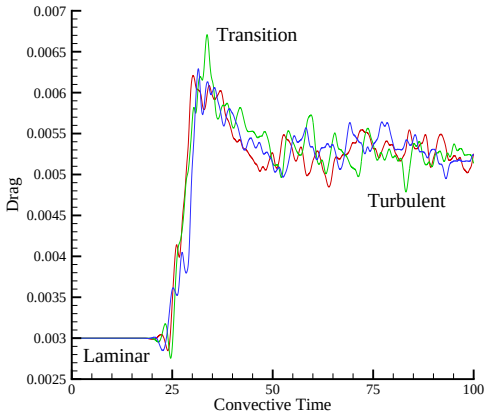

(c)

Figure 12. Wall shear forces on each wall as a function of time for (a) ($Q = M + 1$); (b) ($Q = 2M$); and (c) ($Q = 3M/2$).

even a very coarse grid turbulence simulation may predict the correct statistics – this is the case of the cylinder wake.

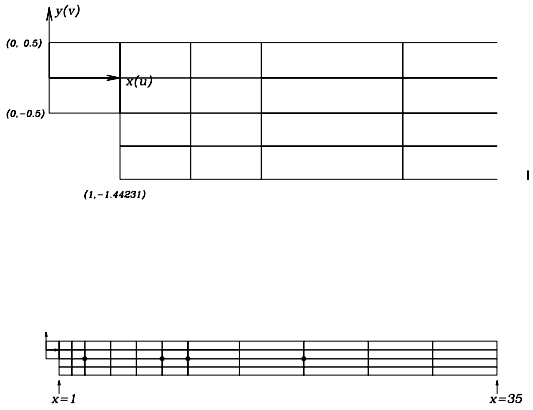

Figure 13. Low resolution mesh for flow over a backwards-facing step.

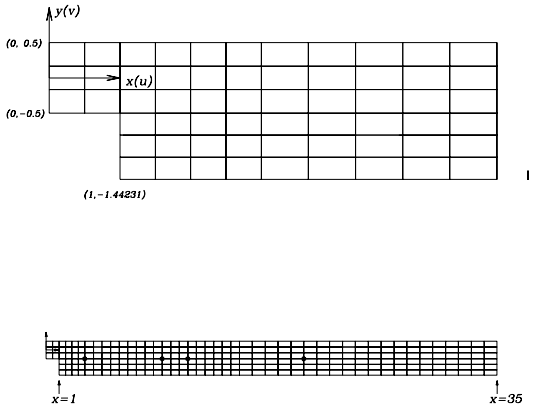

Figure 14. High resolution mesh for flow over a backwards-facing step.

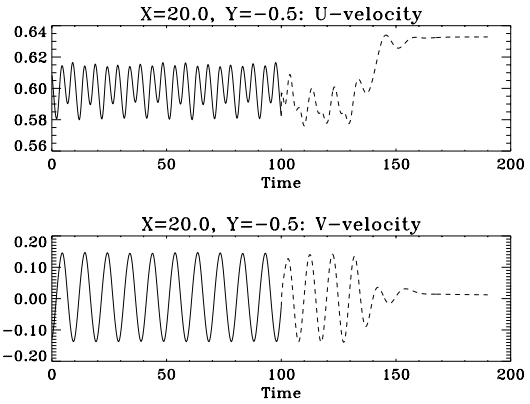

Figure 15. Time history at the third point (shown in the mesh in figures 13 and 14) at Re=700. Solid line: low resolution; Dash line: high resolution.

4.1 Erroneous Flow Transition

The first example is from the systematic spectral simulations presented by ([28]), in the study of bypass transition in a boundary layer. Using a Chebyshev discretization in the inhomogeneous direction and Fourier expansions in the other two directions, they demonstrated that with $P = 33$ Chebyshev modes their simulation showed that a wave structure was present which would give rise to a secondary instability, as suggested earlier by other investigators. However, this structure changed, and the instability vanished completely when $P = 66$ Chebyshev modes were employed in the simulation. In fact, simulations with even higher resolution confirmed this explanation.

An example of similar behavior but with spectral element discretization is the simulation of flow over a backwards-facing step, which was first presented in ([29]). For the resolution shown in figure 13 the flow is unsteady as is evident in the plot that shows time history of velocity (figure 15). However, if higher resolution is used as shown in figure 14, then a steady state is reached (see corresponding figure 15), and this is true even at higher Reynolds numbers up to about $Re \approx 2,500$. Interestingly, the results of the under-resolved simulation are not totally irrelevant as they contain information about the actual flow albeit at a different set of parameters. For example, the two frequencies present in the unsteady case are the natural frequencies of the flow corresponding to the shear layer instability at the step corner and the Tollmien-Schlichting waves in the downstream channel portion. These modes are excited either by background noise, for example, some small turbulence level at the in-

flow, or spontaneously at a higher Reynolds number. Since no absolutely quiet wind tunnels exist, the results of the under-resolved "noisy" simulation, in this case, match the results of the experiment ([30]). We note that other inherently noisy discretizations employing vortex methods and lattice-Boltzmann methods also lead to an unsteady flow solution ([31, 32]).

4.2 Fast-Pitching Airfoil

Next, we consider laminar flow around a rapidly pitching airfoil and compare discontinuous Galerkin spectral/*hp* element results against the finite volume results obtained in ([33]). In particular, we consider a NACA 0015 airfoil pitching upwards about a fixed axis at a constant rate from zero incidence to a maximum angle of attack of approximately 60 degrees. The pivot axis location is at 1/4 of the chord measured from the leading edge. The temporal variation of the pitch given in ([33]) is

$$\Omega(t) = \Omega_0[1 - e^{-4.6t/t_0}], \quad t \geq 0$$

where t_0 denotes the time elapsed for the airfoil to reach 99% of its final pitch rate Ω_0. Here the non-dimensional values are $t_0^* = 1.0$ and $\Omega_0^* = 0.6$ based on the chord length and free stream velocity. As initial condition the computed field at 0 degrees angle of attack is used. The Mach number is $M = 0.2$ and the chord Reynolds number is $Re = 10,000$.

In ([33]) a similar simulation was obtained using a grid fixed to the airfoil by employing an appropriate transformation and discretizing the modified compressible Navier-Stokes equations using the implicit approximate factorization of ([34]). A typical grid used in ([33]) involved 203×101 points. In the present study, we employ the domain shown in figure 16. We performed two different sets of simulations, first with unstructured discretization around the airfoil (see figure 17; total of $3,888$ triangular elements), and subsequently with hybrid discretization with quadrilateral elements around the airfoil for better resolution of boundary layers (total of 116 quadrilateral and 2167 triangular elements). We demonstrate how the hybrid discretization combined with *variable* P-order per element allows accurate resolution of boundary elements without the need for re-meshing. We first performed simulations with constant P-order on all elements and subsequently with higher P-order in the inner layers of elements as shown in figure 18. We contrast the results in figure 19 for P-order $P = 3$ on the left, and P varying from 10 in the innermost layer to 2 in the far field. We see that the boundary layer is unresolved as indicated by the discontinuities at the element interfaces, but it is accurately resolved in the second simulation.

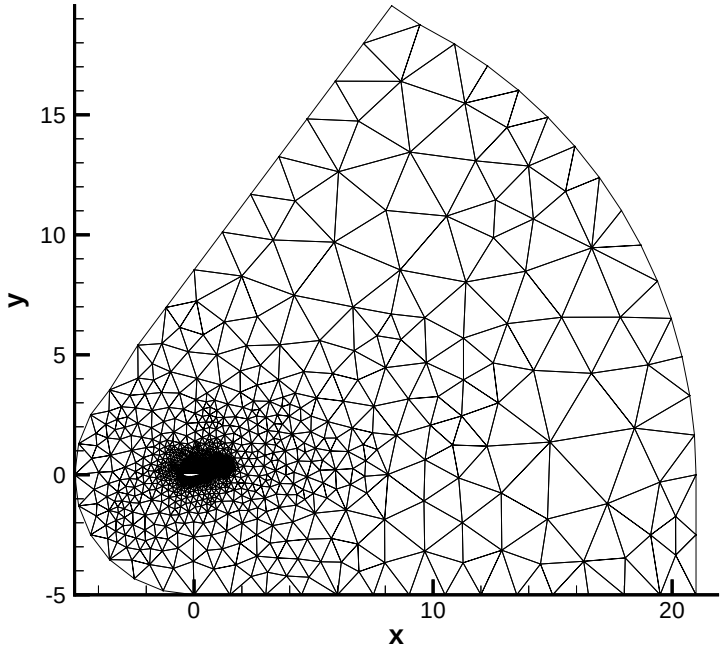

Figure 16. Domain and triangulization for the simulation around the pitching airfoil NACA 0015.

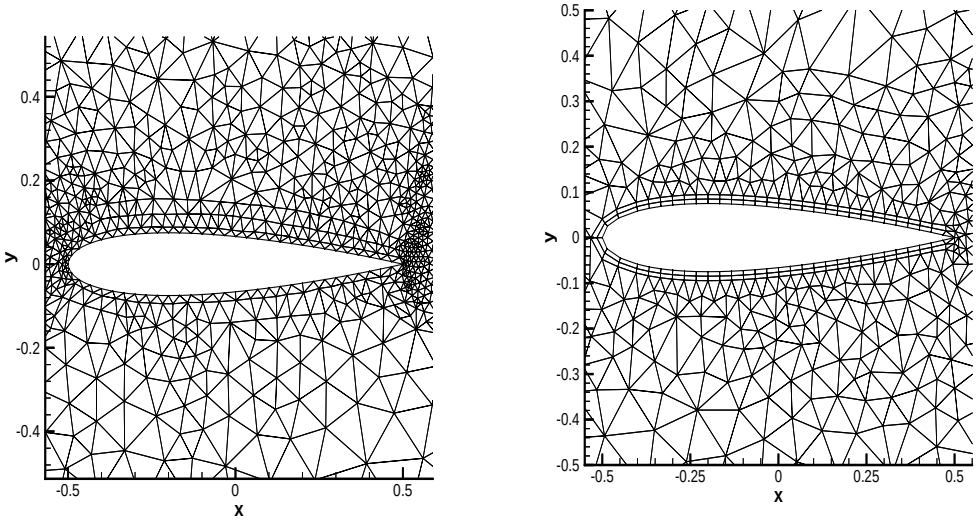

Figure 17. Left: Unstructured discretization consisting of triangles only. Right: Hybrid discretizations consisting of triangles and quadrilaterals. All dimensions are in units of chord length.

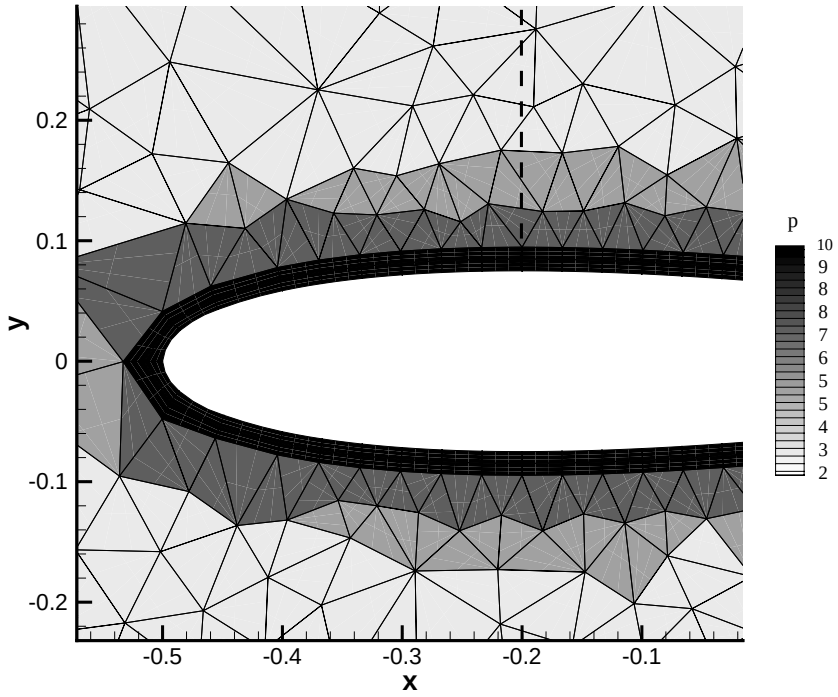

Figure 18. Hybrid discretization showing the variable p-order on a gray-scale map around the airfoil. The dash vertical line indicates the location where boundary layer profiles are taken (see figure 19).

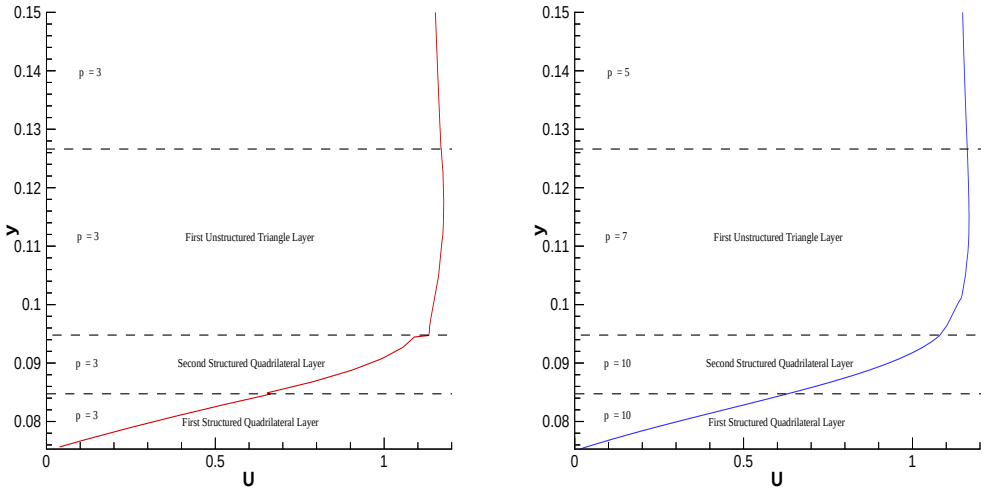

Figure 19. Boundary layer profiles for a simulation with uniform P-resolution (left) and variable P-resolution (right, as shown in figure 18).

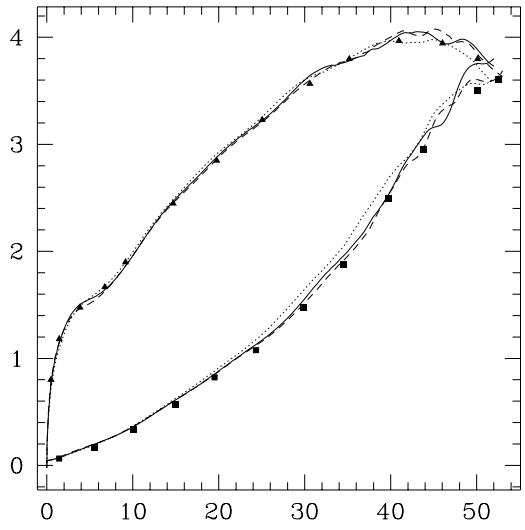

Figure 20. Lift (upper curve) and drag (lower curve) coefficients versus angle of attack in degrees. The symbols correspond to computations of ([33]), the dot line corresponds to our simulation at $P = 2$, the solid line to $P = 3$ and the dash line to $P = 4$.

Returning now to the unstructured grid, we test convergence by also performing P-refinement on the same triangulization but with three different values of spectral order P corresponding to 2nd, 3rd and 4th order polynomial interpolation. In figure 20 we plot the computed lift and drag coefficients versus the angle of attack for grids corresponding to $P = 2, 3$ and $P = 4$. We also include (with symbols) the computational results of ([33]), and we see that in general there is very good agreement except at the large angles of attack close to 50 degrees. This difference is due to qualitative difference in flow structure at small scales, which are only resolved with the higher order simulations.

To examine differences in the flow field due to spatial resolution we plot in figure 21 density contours for the cases $P = 2$ and $P = 3$ at non-dimensional time $t = 0.75$ corresponding to an angle of attack 18.55 degrees. We see that the higher resolution simulation provides a more detailed picture of the vortex shedding in the near-wake, but the contours around the airfoil are very similar. At a later time $t = 1.5$, corresponding to an angle of attack of 44.1 degrees, there are differences between the computations at resolution $P = 2$ and $P = 3$ and these differences are now extended to the upper surface of the airfoil where an interaction between the trailing edge vortex and the upstream propagating shed-

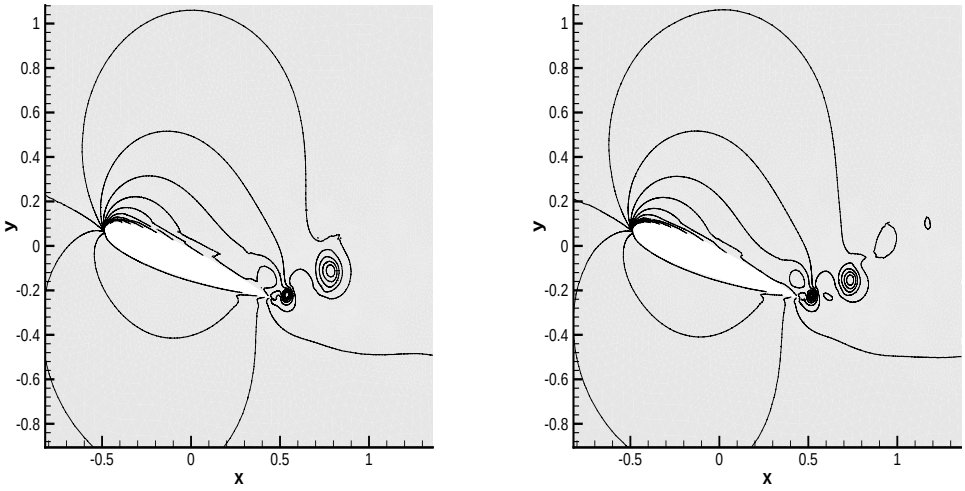

Figure 21. Density contours of the pitching airfoil at non-dimensional time $t = 0.75$ corresponding to 18.55 degrees angle of attack. Shown on the left are contours at spectral order $P = 2$ and on the right at $P = 3$.

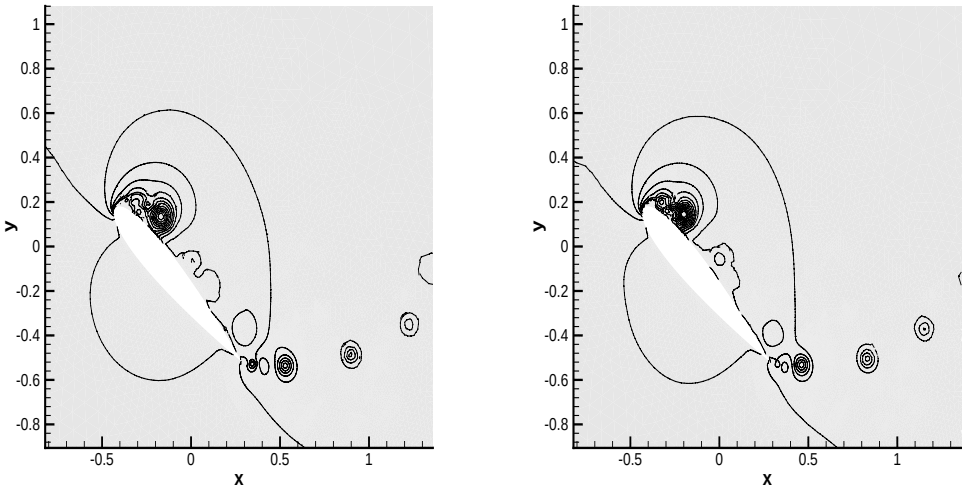

Figure 22. Density contours of the pitching airfoil at non-dimensional time $t = 1.5$ corresponding to 44.1 degrees angle of attack. Shown on the left are contours at spectral order $P = 2$ and on the right at $P = 3$.

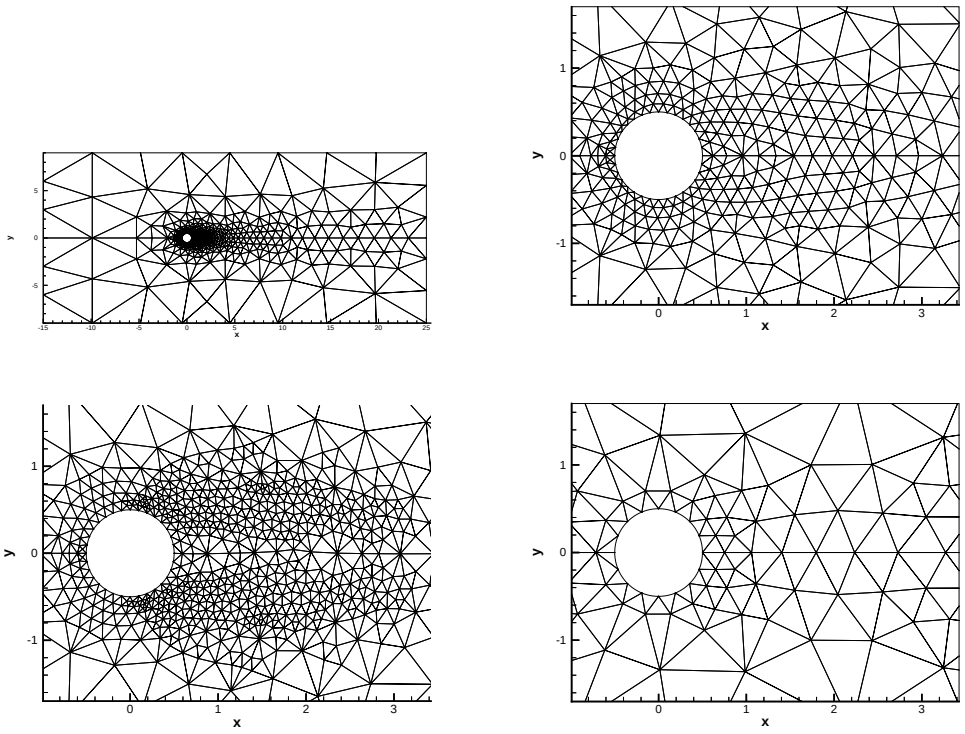

Figure 23. Two-dimensional "z-slice" of the entire domain (top left) and detail around the cylinder of the standard mesh ($K = 902$ elements - top right); refined ($K = 1,622$ elements - bottom left); and coarse mesh ($K = 412$ elements - bottom right) used in the spectral element simulations. The unstructured grid shown is the skeleton based on which hierarchical spectral expansions are constructed.

vortex takes place, as shown in figure 22. These flow pattern differences are responsible for the aforementioned differences in the lift and drag coefficient at large angle of attack as shown in figure 20.

4.3 Turbulent Cylinder Wake

Numerical simulation of turbulent wakes has been computationally prohibitive and only preliminary results have been obtained in ([8]) using DNS. A more systematic study of the cylinder turbulent wake at $Re = 3,900$ was undertaken by ([35]) who used LES with an upwind discretization. A second LES study was performed by ([36]) with central-differencing in order to control the numerical damping reported in the first study, and more recently a high-order LES study was completed

by ([37]). The results from the three studies are similar as far as the computed *mean* and *rms* velocities are concerned, i.e. LES predicts relatively accurately, although not uniformly, the experimental results in the region downstream of $x/D \geq 3$.

However, in the very-near-wake all simulations converge to a mean velocity profile in the *U-shape* unlike the experiments of ([43]) that show a *V-shape*. In contrast, an independent LES study by Rodi and coworkers ([38]) produced a V-shape velocity profile. Also, despite the higher fluctuations sustained in the central-differencing simulations by ([39]), no clear inertial range was obtained in either of the first two LES studies in contrast with the experiments. It is interesting to note that corresponding simulations with the subfilter model turned *off* produced an almost identical spectrum to the LES velocity spectrum. A systematic grid-refinement study performed in ([35]) also suggests that these results are resolution- independent for at least the first ten diameters in the near-wake. The high-order LES of Kravchenko & Moin, however, reproduced accurately the inertial range but predicted the same mean velocity field (i.e. U-shape) as the previous two simulations.

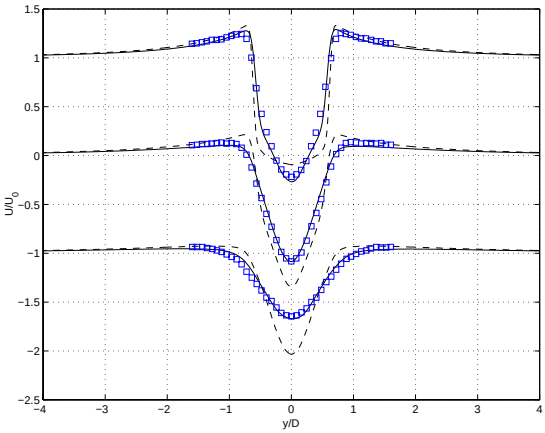

Figure 24. DNS *mean* streamwise velocity predictions at $x/D = 1.06; 1.54; 2.02$ (from top to bottom, respectively), (wide domain - solid line) and (narrow domain - dash line). Squares are data of ([43]).

For the simulations presented here a continuous Galerkin spectral/hp element method was employed in x- and y-directions while a Fourier expansion was employed along the homogeneous direction (cylinder-axis) with appropriate dealiasing. Specifically, triangular elements are used, filled with Jacobi polynomial modes of order P. We performed several simulations corresponding to h-refinement (i.e. with respect to number

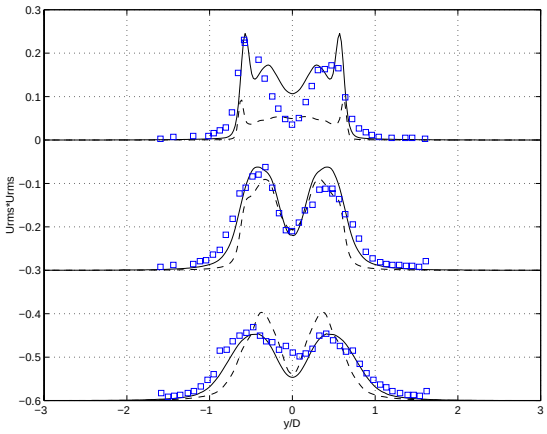

Figure 25. DNS *rms* streamwise velocity predictions at $x/D = 1.06; 1.54; 2.02$ (from top to bottom, respectively). (wide domain - solid line) and (narrow domain - dash line). Squares are data of ([43].

of elements K) and P-refinement (with respect to polynomial order P) ([40]). In figure 23 we show a "z-slice" of the computational domain in the $x - y$ plane with three different discretizations. The top plot shows a grid with $K = 902$ triangular prismatic elements, which has been the standard grid we have used for most cases. In the bottom plot we also show a grid with finer resolution around the shear layers corresponding to $K = 1,622$ elements, and also a grid with coarser resolution corresponding to $K = 412$ elements. The polynomial order per element varied from $P = 4$ to 10, and the number of Fourier modes varied from $N = 2$ to 128 (the corresponding number of physical points is twice the number of modes). The finest resolution simulation employed $K = 902$ elements of order $P = 10$ and 256 points ($N = 128$ Fourier modes) in the spanwise direction. The lowest resolution simulation employed $K = 412$ elements with $P = 6$ and only $N = 2$, i.e. a severe truncation of Fourier modes in the spanwise direction.

The domain extends from $-15D$ at the inflow to $25D$ at the outflow, and from $-9D$ to $9D$ in the cross-flow direction. Neumann boundary conditions (i.e. zero flux) were used at the outflow and on the sides of the domain to minimize the effect of normal boundary layers at the truncated domain. The spanwise length was varied as $L_z/D = \pi/2, \pi, 1.5\pi, 2\pi$. For reference, the spanwise length used in all simulations of ([35, 36, 37]) was $L_z/D = \pi$.

The experimental results of ([41]) suggest a value of correlation length less than $1.5D$ at three diameters downstream; this was obtained using

the streamwise velocity only. However, from plots of the autocorrelation function for all three velocity components and the pressure we have seen that at a centerline point R_{uu} drops to zero at about $1.5D$ but that, in general, at points off-centerline R_{vv} and R_{uu} do not decay as fast ([40]). Such results indicate that values of R_{uu} obtained in experiments at centerline points may under-predict the spanwise correlation length. Therefore, it may be inadequate to use R_{uu} as the only criterion in deciding on the domain size. Indeed, we have found that the span length is very important in determining the *rms* values in the very-near-wake and correspondingly the mean velocity profiles.

In ([40]) high resolution results can be found for many different quantities. Typical velocity profiles for the mean and the variance and for different spans are shown in figures 24 and 25. Here, we examine how such results are affected by *substantially* reducing the grid resolution and without using any subfilter model. In particular, we present here results obtained on the grids shown in figure 23 (bottom right) consisting of $K = 412$ triangular elements and only $P = 6$ and the equivalent $K = 902$ and $P = 4$, both cases corresponding to approximately the same number of degrees of freedom. More comparisons with the subfilter model on the same grid can be found in ([42]). We will first use only *two Fourier modes* in the span, i.e. the mean mode and one perturbation ($N = 2$ or 4 points). We also choose a small value for the spanwise length $L_z/D = \pi/2$.

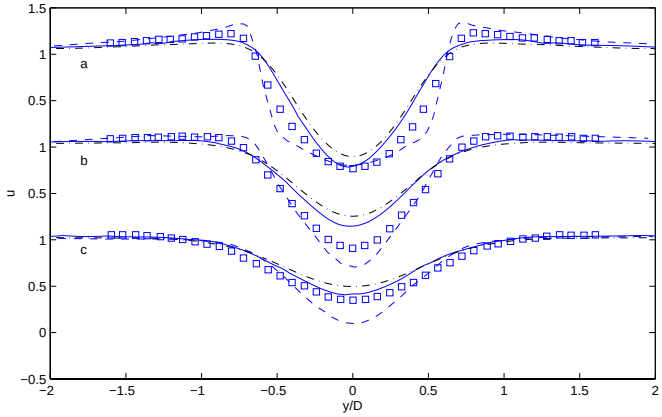

Figure 26. Streamwise mean velocity profile at $x/D = 1.06, 1.54, 2.02$. Squares denote experimental data of ([43]), solid line DNS ($K = 412$; $P = 6$), dash-dot line DNS ($K = 902$; $P = 4$) and dash line LES of Beaudan & Moin ([35]).

We compare first with the experiments of ([43]) in the very near-wake and subsequently with the experiments of ([41]) farther downstream.

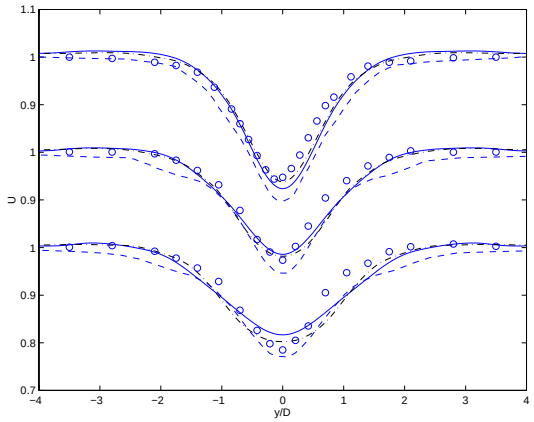

Figure 27. Mean velocity profiles at $x/D = 4, 7, 10$. Circles denote experimental data of ([41]), solid line DNS ($K = 412$; $P = 6$), dash-dot line DNS ($K = 902$; $P = 4$) and dash line LES of Beaudan & Moin ([35]).

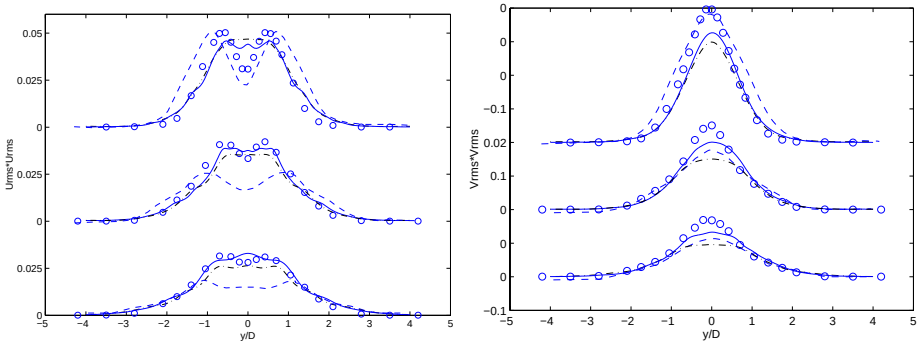

Figure 28. Left: Turbulent intensity of the streamwise velocity (u^2_{rms}) at $x/D = 4, 7, 10$. Right: Turbulent intensity of the cross-flow velocity (v^2_{rms}) at $x/D = 4, 7, 10$. Circles denote experimental data of Ong & Wallace, solid line DNS ($K = 412$; $P = 6$), dash-dot line DNS ($K = 902$; $P = 4$) and dash line LES of Beaudan & Moin ([35]).

In figure 26 we plot the mean streamwise velocity profile at locations $x/D = 1.06, 1.54$ and 2.02. We also include the experimental data of ([43]) taken from ([35]), and the LES data of ([35]). We see that the predictions from both low-resolution simulations without subfiltering are comparable to the LES predictions. In figures 27, 28 we plot the mean streamwise velocity and turbulent fluctuations, respectively, at locations $x/D = 4, 7, 10$ and compare with the experimental data of ([41]). The predictions for the mean velocities are good but the streamwise turbulence intensity shows some wiggles, which is an indication of insufficient resolution. However, the low-resolution spectral simulations obtain an

overall better agreement with the experimental data than the dissipative LES predictions reported in ([35]).

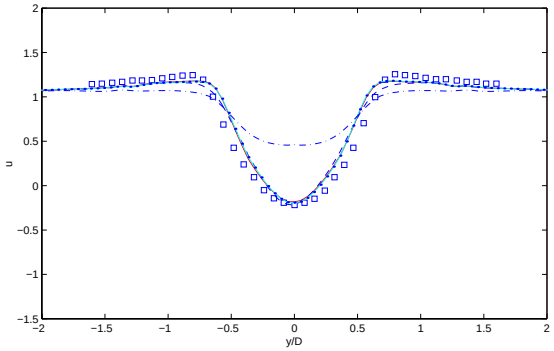

Figure 29. Streamwise mean velocity profile at $x/D = 1.06$ for different Fourier modes employed along the span. Squares denote experimental data of ([43]), dash-dot line 2D simulation, dash line $N = 2$, dot-solid line $N = 8$ and solid line $N = 32$ (coincides with $N = 8$).

The results presented so far were obtained with only $N = 2$ Fourier modes employed along the cylinder span. Of interest is to examine the influence of the number of Fourier modes N on the mean velocity profiles presented above while retaining the same resolution in the $x - y$ planes. We performed additional simulations with $N = 8$ and 32 and also a two-dimensional simulation. As we see in figure 29 there is essentially no difference in the predicted mean *streamwise* velocity profile from $N = 2$ to $N = 32$ but the two-dimensional prediction deviates substantially. The cases with $N = 8$ and $N = 32$ correspond to almost identical predictions suggesting convergence in the z-direction.

The results presented here indicate that the first Fourier mode carries most of the spanwise energy for the chosen span $L_z/D = \pi/2$, as it is evident by comparing with the two-dimensional results in figure 29. This has been independently verified by computing the averaged plane-modal energy $E_{xy}(m) = \int_{xy}[u_m^2 + v_m^2 + w_m^2]dxdy$ and observe its decay with respect to the mode number.

Given the surprisingly good results with this low-resolution at $Re = 3,900$, we performed another set of simulations with the same low-resolution and with only $N = 2$ Fourier modes at $Re = 5,000$ for which we had available experimental data from the work of ([44]). In figure 30 we plot the mean velocity profile and the streamwise turbulent intensity $\overline{u'^2}$ at station $x/D = 10$. Again, we see that despite some wiggles in the numerical results the agreement with the experimental results is good.

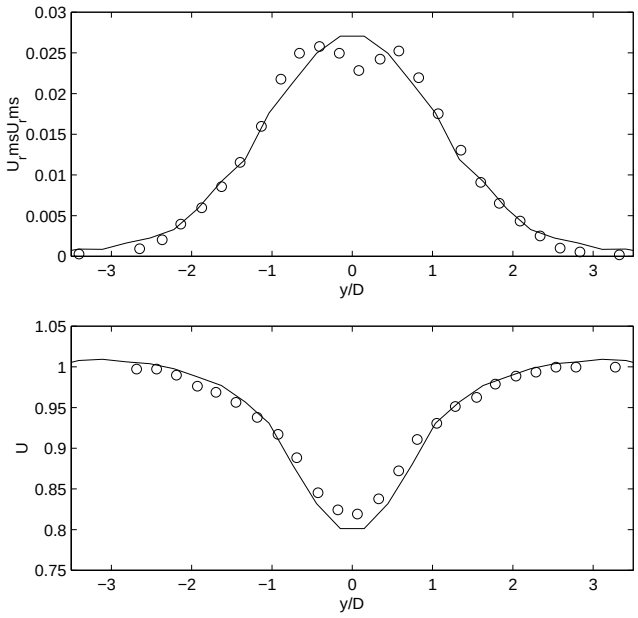

Figure 30. Streamwise mean velocity profile (bottom) and turbulent fluctuation (top) at $x/D = 10$ and $Re = 5,000$. The experimental data (circles) are from Zhou & Antonia (1993).

5. Discussion

Spectral methods have been used with great success in simulating turbulent flows in periodic cubes and channel domains. The algorithmic developments of the last two decades have led to a new simulation capability for complex-geometry turbulent flows as well. Such capability, in conjunction with terascale computing at the PC cluster level, will undoubtly lead to significant advances in simulating turbulence in more realistic configurations and in realistic operating conditions. In this chapter, we have summarized some of these developments and have presented results for several transitional and turbulent flows in complex-geometry domains.

Great care has to be exercised however in interpreting results from DNS or LES in simple-geometry flows at high Reynolds number or in complex-geometry flows with new physics. Many of these simulations may be under-resolved at some level; for example, although the velocity mean and variance may be correctly predicted, the high-order statistics or the dissipation spectrum may be erroneous. It is important, therefore, to have a diverse set of diagnostic tools to characterize numerical uncer-

tainty in these situations. In particular, understanding how numerical methods behave in DNS and LES for many prototype flows provides an insight into uncertainities and their origin in large-scale simulations. Validation and verification ([1]) of a turbulent simulation is a very difficult task that, unfortunately, cannot be handled solely by error estimators which are based primarily on extensions of linear concepts ([45, 46, 47]).

Under-resolved simulations are not useless if the numerical uncertainty is properly characterized ([48, 49, 50]), i.e. quantified with a properly constructed error bar ([51]). In many cases such under-resolved simulations may contain the answer that we seek, e.g. an averaged lift or drag coefficient and at the accuracy level that we expect. The type of flow that we simulate is important in that respect. We have presented here, for example, low-resolution simulations of the cylinder turbulent wake which lead to results that match the experiments at $Re = 5,000$. Flows with inherent low-dimensionality, such as the cylinder wake for which the vortex shedding process dominates the dynamics, may then be easier to simulate. Moreover, quantification of numerical uncertainty in hierarchical methods, such as the spectral/hp element method, is also easier to achieve and offer the possibility of obtaining multiple solutions with relatively simple P-refinement without the need for re-meshing which, typically, is a large overhead component in a turbulence simulation.

Acknowledgments

This work was supported by ONR, AFOSR, DOE, DARPA and NSF. It is based partially on findings in the Ph.D theses of S.J. Sherwin, I. Lomtev and X. Ma. The simulations were performed on the IBM SP2/3 at the San Diego Supercomputing Center (NPACI), at the Maui High Performance Computing Center, at the Brown University Center for Scientific Computing and Visualization, and on the SGI Origin 2000 at the NCSA, University of Illinois at Urbana Champaign.

References

[1] P.J. Roache: 1998. Verification and validation in computational space and engineering. *Hermosa*.

[2] R. Zores: 1989. Numerische untersuchungen met einem grobauflosenden simulationsmodell fur die turbulente kanalstromung. *Institut fur Theoretische Stromungsmechanik*. DLR-Gotting-Germany

[3] G.E. Karniadakis, S.A. Orszag: 1993. Nodes, modes and flow codes. *Physics Today* **46**, 34.

[4] S. Ghosal, P. Moin: 1995. The basic equations for the large-eddy simulation of turbulent flow in complex geometry. *J. Comp. Phys.* **118**, 24.

[5] G.E. Karniadakis, S.J. Sherwin: 1999. Spectral/hp element methods for CFD. *Oxford University Press*.

[6] A.T. Patera: 1984. A spectral method for fluid dynamics: laminar flow in a channel expansion. *J. Comp. Phys.* **54**, 468

[7] D.C. Chu, G.E. Karniadakis: 1993. A direct numerical simulation of laminar and turbulent flow over riblet-mounted surfaces. *J. Fluid Mech.* **250**, 1

[8] R.D. Henderson, G.E. Karniadakis: 1995. Unstructured spectral element methods for simulation of turbulent flows. *J. Comp. Phys.* **122**, 191

[9] S.J. Sherwin, G.E. Karniadakis: 1995. A triangular spectral element method; applications to the incompressible Navier-Stokes equations. *Comp. Meth. Appl. Mech. Eng.* **23**, 83

[10] S.J. Sherwin, G.E. Karniadakis: 1995. A new triangular and tetrahedral basis for high-order finite element methods *J. Num. Meth. Eng.* **38**, 3775

[11] D.J. Mavripilis, V. Venkatakrishnan: 1995 A unified multigrid solver for the Navier-Stokes equations on mixed element meshes. *AIAA-95-1666, San Diego, CA*

[12] V. Parthasarathy, Y. Kallinderis, K. Nakajima: 1995. Hybrid adaptation method and directional viscous multigrid with presmatic-tetrahedral meshes. *AIAA-95-0670, Reno, NV*.

[13] G.E. Karniadakis, M. Israeli, S.A. Orszag: 1991. High-order splitting methods for the incompressible Navier-Stokes equations. *J. Comp. Phys.* **97**, 414

[14] N.A. Petterson: 2001. Stability of pressure boundary conditions for Stokes and Navier-Stokes equations. *J. Comp. Phys.* **172**, 40

[15] B. Cockburn, G.E. Karniadakis, C.W. Shu: 2000. The development of discontinuous Galerkin methods. *Discontinuous Galerkin methods: Theory, Computation and Applications*, Springer-Verlag

[16] D. Xiu, G.E. Karniadakis: 2001. A Semi-Lagrangian High-Order Method for Navier-Stokes Equatins, *J. Comp. Phys.*, **172**, 658-684.

[17] I. Lomtev, G. Quillen, G.E. Karniadakis: 1998. Spectral/hp methods for viscous compressible flows on unstructured 2D meshes. *J. Comp. Phys.* **144**, 325

[18] C. Johnson: 1994. Numerical solution of partial differential equations by the finite element method. *Cambridge University Press*

[19] G. Jiang, C.W. Shu: 1994. On a cell entropy inequality for discontinuous Galerkin methods. *Math. Comp.* **62**, 531

[20] R.M. Kirby: 2002. Dynamic spectral/hp refinement: algorithms and applications to flow-structure interactions. *PhD-thesis: Brown University: applied mathematics*

[21] R. Verstappen, A. Veldman: 2002. Preserving symmetry in convection-diffusion schemes. *This volume*

[22] W. Couzy: 1995. Spectral element discretization of the unsteady Navier-Stokes equations and its iterative solution in parallel computers. *PhD-thesis: Ecole Polytechnique Federale de Lausanne*

[23] E.M. Ronquist: 1996. Convection treatment using spectral elements of different order. *Int. J. Numer. Methd. Fluids* **22**, 241

[24] I. Lomtev, C. Quillen, G.E. Karniadakis: 1998. A discontinuous Galerkin ALE method for compressible viscous flow in moving domains. *J. Comp. Phys.* **155**, 128

[25] E. Tadmor: 1989. Convergence of spectral methods for nonlinear conservation laws. *SIAM J. Numer. Anal.* **26**, 30

[26] G.S. Karamanos, G.E. Karniadakis: 2000. A spectral vanishing viscosity method for large-eddy simulations. *J. Comp. Phys.* **162**, 22

[27] E. Tadmor: 1993. Total variation and error estimates for spectral viscosity approximations. *Math. Comp.* **60**, 245

[28] D.S. Henningson, A. Lundblach, A.V. Johansson: 1993. A mechanism for bypass transition from localized disturbances in wall-bounded shear flows. *J. Fluid Mech.* **250**, 169

[29] L. Kaiktsis, G.E. Karniadakis, S.A. Orszag: 1991. Onset of three-dimensionality, equilibria, and early transition in flow over a backward-facing step. *J. Fluid Mech.* **191**, 501

[30] L. Kaiktsis, G.E. Karniadakis, S.A. Orszag: 1996. Unsteadiness and convective instabilities in two-dimensional flow over a backward-facing step. *J. Fluid Mech.* **321**, 157

[31] J.A. Sethian, A.F. Ghoniem: 1988. Validation of vortex methods. *J. Comp. Phys.* **74**, 283

[32] Y.H. Qian and S. Succi and F. Massaioli and S.A. Orszag: 1993. A benchmark for lattice BGK model: flow over a backward-facing step. *Pattern formation and lattice-gas automata* A. Lawniczak, R. Kapral (Eds.), June 7-12, Waterloo.

[33] M.R. Visbal, J.S. Shang: 1989. Investigation of the flow structure around a rapidly pitching airfoil. *AIAA J.* **27**, 1044

[34] R. Beam, R. Warming: 1978. An implicit factored scheme for the compressible Navier-Stokes equations. *AIAA J.* **16**, 393

[35] P. Beaudan, P.Moin: 1994. Numerical experiments on the flow past a circular cylinder at sub-critical Reynolds number. *Report No. TF-62, Stanford University*

[36] R. Mittal, P. Moin: 1996. Large-eddy simulation of flow past a circular cylinder. *APS Bulletin: 49-th CFD Meeting* **41**

[37] A.G. Kravchenko, P. Moin: 1998. B-spline methods and zonal grids for numerical simulations of turbulent flows. *Stanford University: Report No. TF-73*

[38] J. Frohlich, W. Rodi, Ph. Kessler, S. Parpais, J.P. Bertoglio, D. Laurence: 1998. Large-eddy simulation of flow around circular cylinders on structured and unstructured grids. *Notes on numerical fluid mechanics* E.H. Hirschel (Ed.)

[39] R. Mittal: 1996. Progress on LES of flow past a circular cylinder. *CTR Annual research briefs, Stanford*, 233

[40] X. Ma, G.S. Karamanos, G.E. Karniadakis: 2000. Dynamics and low-dimensionality in the turbulent near-wake. *J. Fluid Mech.* **410**, 29

[41] L. Ong, J. Wallace: 1996. The velocity field of the turbulent very near wake of a circular cylinder. *Experiments in fluids* **40**, 441

[42] G.S. Karamanos: 1999. Large eddy simulation using unstructured spectral/hp elements. *PhD-thesis: Imperial College*

[43] L.M. Lourenco, C. Shih: Characteristics of the plane turbulent near wake of a circular cylinder. A particle image velocimetry study. (Unpublished results taken from Beaudan and Moin 1994.)

[44] Y. Zhou, R.A. Antonia: 1993. A study of turbulent vortices in the near wake of a cylinder. *J. Fluid Mech.* **253**, 643

[45] T.J. Oden, W. Wu, M. Ainsworth: 1994. An a porsteriori error estimate for finite element approximations of the Navier-Stokes equations. *Comp. Meth. Appl. Mech. Eng.* **111**, 185

[46] L. Machiels, J. Peraire, A.T. Patera: 2001. A posteriori finite element output bounds for the incompressible Navier-Stokes equations: applications to a natural convection problem. *J. Comp. Phys.*, to appear

[47] M. Ainsworth, T.J. Oden: 2000. A posteriori error estimation in finite element analysis. *John Wiley & Sons*

[48] A.J. Chorin, A.P. Kast, R. Kupferman: 1998. Optimal prediction of underresolved dynamics. *Proc. Natl. Acad. Sci. USA* **95**, 4094

[49] Y. Maday and A.T. Patera and J. Peraire: 1999. A general formulation for a posteriori bounds for output functionals of partial differential equations. *C.R. Acad. Sci. Paris, Series I*, **328**, 823

[50] J. Glimm, D.H. Sharp: 1999. Prediction and the quantification of uncertainty. *Physica D* **133**, 152

[51] G.E. Karniadakis: 1995. Towards an error bar in CFD. *J. Fluids Eng.* **117**